Chemical Science

ROYAL SOCIETY OF CHEMISTRY

EDGE ARTICLE

View Article Online
View Journal | View Issue

Cite this: *Chem. Sci.*, 2025, **16**, 19130

All publication charges for this article have been paid for by the Royal Society of Chemistry

Received 21st April 2025
Accepted 5th August 2025

DOI: 10.1039/d5sc02892b

rsc.li/chemical-science

Ambidextrous fine-tuning of zeolite-like hydrogen-bonded organic frameworks (HOFs) *via* scalable green synthesis for efficient biogas upgrading

Baobing Tang,[a] Xueyue Yu,[a] Guanghua Li,[a] Xin Liu, *[c] Jiantang Li *[b] and Yunling Liu *[a]

Zeolite-like supramolecular assemblies (ZSAs) are a distinctive class of hydrogen-bonded organic frameworks (HOFs) that form zeolite-like structures using fundamental four-membered ring (4 MR) building units, known as metal–organic squares (MOSs). Herein, we developed a zeolite-like supramolecular assembly (ZSA) platform to precisely control hydrogen-bond directionality, coupled with confinement effects, ultimately synthesizing two isoreticular HOFs, **ZSA-12** and **ZSA-13**, with distinct pore environments. Notably, owing to their microporous structures, **ZSA-12** and **ZSA-13** exhibited exceptional CO_2 adsorption capacity and ultra-high CO_2/CH_4 separation selectivity. The IAST selectivity value of 94.8 sets a benchmark, surpassing that of all previously reported HOFs. Theoretical calculations and breakthrough experiments confirmed the outstanding separation capability of **ZSA-12** and **ZSA-13**, both of which also demonstrated remarkable thermal and chemical stability. Furthermore, gram-scale synthesis of **ZSA-12** and **ZSA-13** was successfully achieved under mild conditions using pure water as the solvent—one of the few reported HOFs that can be synthesized in large quantities *via* a water-based process at an exceptionally low cost. Thus, **ZSA-12** and **ZSA-13** offer a new strategy for the synthesis of isoreticular HOFs and hold great promise for biogas purification and upgrading applications.

Introduction

Biogas, a cost-effective renewable energy source produced by the anaerobic digestion of organic waste, is considered a key transitional energy in the shift toward sustainable energy. Currently, biogas directly supplies 10–14% of the global energy demand, with projections indicating an increase to 25% in the near future.[1,2] The main components of biogas are CH_4 (50–80%) and CO_2 (20–50%), with their ratio determined by the type of organic feedstock. Before biogas can be injected into natural gas pipelines, it must be upgraded to achieve a CH_4 concentration of over 97%.[3,4] Therefore, developing cost-effective CO_2 separation methods is a critical challenge in the energy sector.[5,6] In recent years, porous materials have attracted significant attention due to their excellent adsorption performance and energy-saving potential.[7–11] However, an ideal adsorbent must not only exhibit high CO_2 selectivity but also balance adsorption capacity, stability, recyclability, and economic feasibility to meet practical application needs. Thus, designing adsorbents with both high separation performance and industrial applicability remains a key challenge in this field.[12,13]

Hydrogen-bonded organic frameworks (HOFs), as a subset of porous framework materials, represent a class of crystalline porous materials assembled *via* intermolecular hydrogen bonding.[14,15] Due to the intrinsic properties of hydrogen bonds, HOFs exhibit unique characteristics distinct from those of conventional porous materials such as zeolites, metal–organic frameworks (MOFs), and covalent organic frameworks (COFs). These distinctive features include high structural diversity, exceptional flexibility, mild synthesis conditions, ease of recrystallization, and self-healing capability.[16–19] In particular, HOFs with permanent porosity have experienced rapid development in recent years and have found widespread applications in areas such as gas adsorption and separation,[20–23] biomedicine,[24–27] and catalysis.[28–31]

The functionalization of HOFs faces several challenges, primarily due to their relatively weak hydrogen bonding interactions, which can lead to structural instability under certain conditions such as humidity or solvent exchange.[32] Additionally, precise control over the incorporation of functional groups without disrupting the hydrogen-bonding net remains difficult, resulting in uneasy to get the functionalized isoreticular structures.[33,34] The reversible nature of hydrogen

[a]*State Key Laboratory of Inorganic Synthesis and Preparative Chemistry, College of Chemistry, Jilin University, Changchun 130012, P. R. China. E-mail: yunling@jlu.edu.cn*

[b]*Key Laboratory of the Ministry of Education for Advanced Catalysis Materials, College of Chemistry and Materials Science, Zhejiang Normal University, Jinhua 321000, P. R. China. E-mail: jiantang.li@zjnu.edu.cn*

[c]*School of Chemistry, Dalian University of Technology, Dalian 116000, P. R. China. E-mail: xliu@dlut.edu.cn*

bonds also poses challenges in achieving long-term stability, particularly for applications requiring chemical resistance.[35] Moreover, compared to COFs or MOFs, HOFs often exhibit limited tunability in terms of porosity and functional group attachment, restricting their applicability in some specific fields.[36,37]

Compared to single-component HOFs, the mixed-moiety approach, though rarely reported, offers significant potential for expanding both the functionalization and isoreticular extension of HOFs. For example, HOFs constructed using guanidinium sulfonate (GS) moieties benefit from the fact that hydrogen bonds primarily form between guanidinium and sulfonate groups, allowing greater flexibility in the selection of carboxylate ligands with varying lengths and symmetries. This tunability enables the design of a diverse range of GS-HOFs with tailored pore sizes.[38] Not only is the construction of mixed-moiety HOFs inherently challenging, but further functionalization of the building units can also disrupt the hydrogen-bonding nets, making isoreticular chemistry extremely difficult to achieve. In this regard, the incorporation of metal ions to stabilize structural units in HOFs, as seen in HOF-21, is an effective strategy.[39,40] In HOF-21, Cu stabilizes paddle-wheel SBUs, improving rigidity, preventing collapse, and maintaining tunability, enabling gas separation applications and supporting the development of more robust and functional HOFs.

One unique strategy proposed by our team is the construction of discrete 0D MOS, which are made up of three components: metals, bridging ligands, and capping ligands (Fig. S1). The intrinsic nature of the mixed-moiety construction in MOS enables the independent differentiation of hydrogen bond donors (amino group) and acceptors (carboxylic group), thereby ensuring the directional assembly of hydrogen bonding. This unique characteristic allows for the targeted construction of zeolite-like HOFs, which are referred to as zeolite-like supramolecular assemblies (ZSAs). The most representative example is the **ZSA-1** platform with **gis** topology, in which the MOS was constructed through the assembly of Co(III) with 4,5-imidazoledicarboxylate (H_3ImDC) ligands and 1,2-propylenediamine (1,2-PDA). The saturated coordination bonds in **ZSA-1** endow this platform with exceptional thermal and pH stability, while the multi-connected hydrogen-bonding imparts unique flexibility to the structure.[41] Notably, the well-defined hydrogen-bonding interactions in different MOSs ensure that functional modifications of the two independent components within the MOS do not disrupt the overall hydrogen-bonding net. Structurally, substitutions at the 2-position of the H_3ImDC ligand significantly increase steric effects along the z direction, while the incorporation of larger bis(monodentate) diamine capping ligands expands the steric environment in the $x + y$ direction. The simultaneous regulation in both directions enables a systematic fine-tuning of the pore environment in the **gis** platform (Scheme 1).

In addition to the pursuit of gas separation performance, low-cost large-scale synthesis is also a critical step towards the commercialization of HOFs. However, HOFs are typically synthesized using expensive monomers and inevitably involve the use of toxic and harmful organic solvents, which has become another limiting factor in their development.[42,43] To date, there have been few reports on the large-scale synthesis of low-cost HOFs. Furthermore, due to the poor solubility of ligands in water, the synthesis of HOFs in pure water is even rarer. This highlights the need to develop HOFs that balance synthesis cost-effectiveness and high separation performance, which will significantly advance their development.

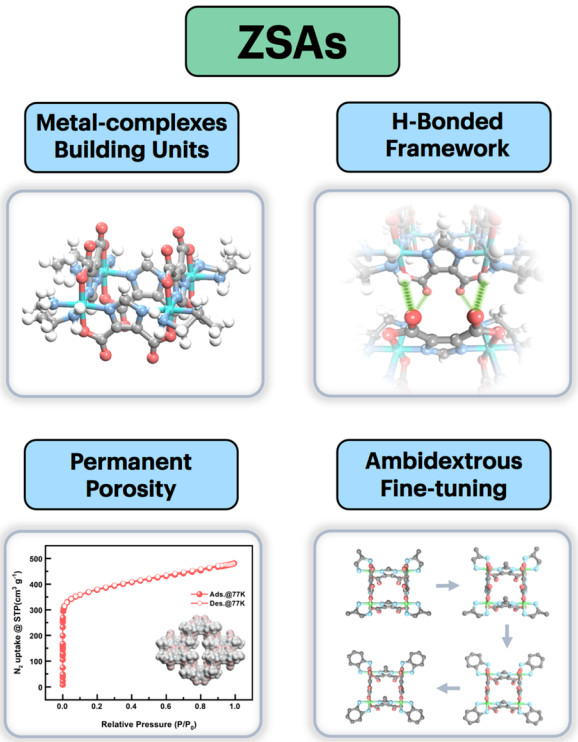

Scheme 1 Structural characteristics of ZSAs.

In this work, we successfully synthesized two additional isoreticular **gis**-type HOFs based on **ZSA-1** and **ZSA-3**. First, 1,2-diaminocyclohexane (1,2-DACH) was used to replace 1,2-diaminopropane (1,2-PDA) in $Co_4[(H_3ImDC)_4(1,2\text{-}PDA)_4]$ (**ZSA-1**), resulting in $Co_4[(H_3ImDC)_4(1,2\text{-}DACH)_4]$ (**ZSA-12**). Then, using a ligand functionalization strategy, a methyl group was introduced at position 2 of the organic ligand 4,5-imidazolidine dicarboxylic acid (H_3ImDC), yielding $Co_4[(H_3MeImDC)_4(1,2\text{-}PDA)_4]$ (**ZSA-3**) and $Co_4[(H_3MeImDC)_4(1,2\text{-}DACH)_4]$ (**ZSA-13**). As expected, we achieved precise control over the pore size and successfully synthesized confined micropores. Notably, compared to most materials reported in the literature, **ZSA-12** and **ZSA-13** exhibited outstanding CO_2/CH_4 separation selectivity. Both **ZSA-12** and **ZSA-13** demonstrated excellent separation performance in breakthrough experiments at varying ratios and flow rates. Furthermore, their separation efficiency remained stable over at least five cycles. Additionally, **ZSA-12** and **ZSA-13** can be successfully synthesized in gram quantities in water, with a cost of only $0.62 per gram. These results highlight the potential of **ZSA-12** and **ZSA-13** as benchmark HOFs for biogas upgrading.

Results and discussion

Structure design and description

Single-crystal X-ray diffraction analysis reveals that **ZSA-1**, **ZSA-3**, **ZSA-12**, and **ZSA-13** form an isoreticular series of zeolite-like hydrogen-bonded organic frameworks, all crystallizing in the $I4_1/amd$ space group. These structures are constructed using metal–organic squares (MOSs) as fundamental building blocks, which self-assemble into a **gis** zeolitic topology *via* directional hydrogen bonding. Taking **ZSA-1** as an example, its MOS unit consists of four hexacoordinated Co ions, four H_3ImDC bridging ligands, and four 1,2-PDA capping ligands, precisely assembled into a well-defined structural motif. A key structural design feature is the explicit differentiation of hydrogen bond donors and acceptors within the MOS unit: the amino groups of the capping ligands act as hydrogen bond donors, while the carboxyl groups of the bridging ligands act as acceptors (Fig. S2–S5). This arrangement establishes a highly predictable N–H···O hydrogen bonding network, which drives the self-assembly of the framework. Within the structure, six MOSs are arranged in a 1–2–2–1 parallel configuration, forming orthogonal channels that extend throughout the framework (Fig. 1). Based on this structural insight, we propose a fine-tuning approach in which the $x + y$ direction is defined by the diagonal connection of capping ligands within the MOS unit, while the z direction corresponds to the axial orientation of the bridging ligands (Fig. 1a). By synergistically modulating both the $x + y$ direction and the z direction, we achieve precise control over pore size. Specifically, **ZSA-3** is modified along the z direction by replacing the bridging ligand H_3ImDC with H_3MeImDC, introducing steric hindrance along this direction and thereby reducing the pore size from 5.8 Å × 11.7 Å to 6.1 Å × 8.7 Å (the length and width of the minimum bounding rectangle in the orthogonal projection of the pore). In **ZSA-12**, pore size is further reduced to 4.0 Å × 12.0 Å by increasing the size of the capping ligands, thereby introducing steric hindrance within the $x + y$ direction. **ZSA-13** incorporates a dual modulation approach, simultaneously tuning the $x + y$ direction and z direction. By employing H_3MeImDC as the bridging ligand and 1,2-DACH as the capping ligand, the synergistic optimization of the pore size is achieved, resulting in the smallest pore size of 4.1 Å × 4.1 Å (Fig. 1b). Due to the irregular shape of the pore channels, the effective size in the actual adsorption process may be smaller than the estimated value, resulting in a stronger confinement effect than expected. Experimental PXRD patterns exhibit excellent agreement with theoretical simulations (Fig. S6–S9), confirming the high phase purity of **ZSA-1**, **ZSA-3**, **ZSA-12**, and **ZSA-13**. The successful implementation of the ambidextrous fine-tuning strategy enables precise regulation of ZSA pore dimensions, laying a robust structural foundation for the enhancement of gas separation performance.

Gas adsorption measurements

The ambidextrous fine-tuning of the ZSA platform along both the $x + y$ and z directions endows its pore environment with high adjustability, which is also reflected in its highly tunable gas adsorption performance. Prior to gas adsorption measurements, the ZSAs were subjected to ethanol solvent exchange for

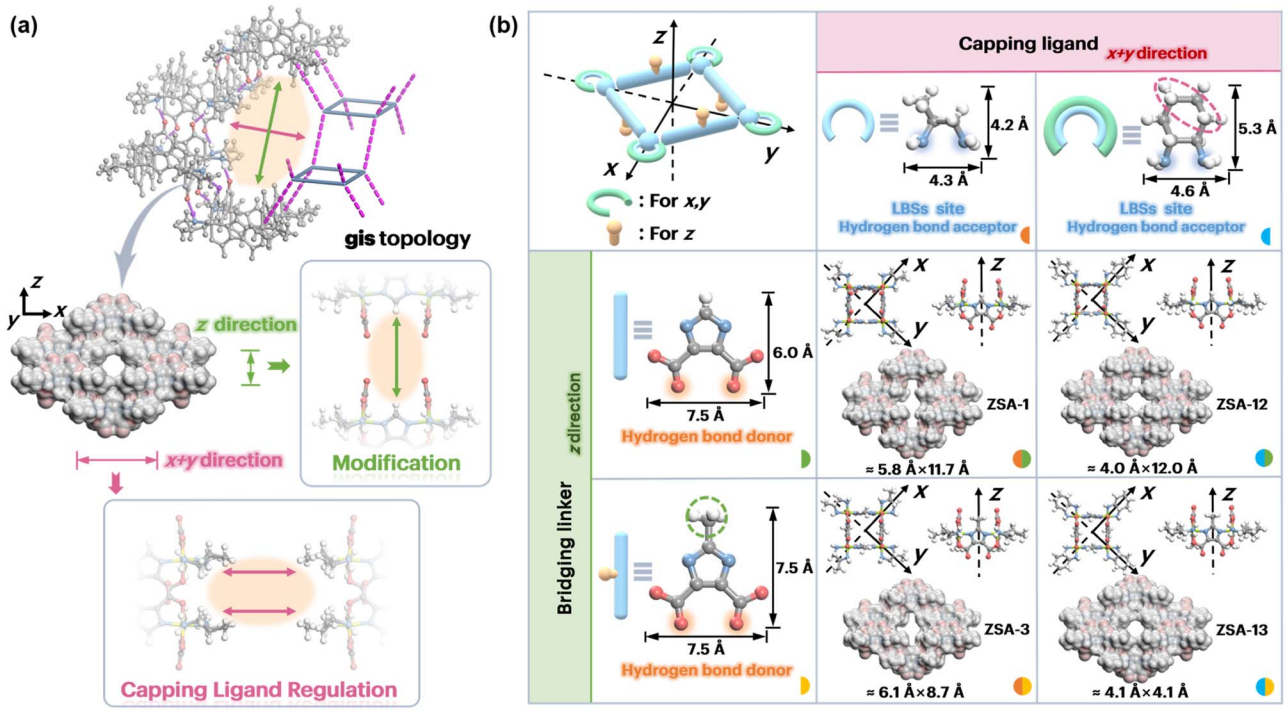

Fig. 1 (a) Schematic illustration of the hydrogen-bonding, topology, and pore regulation in ZSAs; (b) x, y, and z axes in the MOS, showing the dimensions of the bridging and capping ligand and the pore sizes in the ZSAs.

72 hours followed by thermal activation. PXRD patterns confirmed that all ZSAs retained structural stability after activation (Fig. S6–S9). TGA results indicated that all ZSAs were successfully activated (Fig. S10–S13). Subsequently, N_2 adsorption measurements were conducted at 77 K for four ZSAs. The results revealed that as the steric hindrance of the coordinating ligand increased, the N_2 adsorption capacity and BET surface area gradually decreased. **ZSA-1**, **ZSA-3**, **ZSA-12**, and **ZSA-13** exhibited N_2 uptake and BET surface area values of 402 $cm^3\ g^{-1}$ and 1331 $m^2\ g^{-1}$, 342 $cm^3\ g^{-1}$ and 1103 $m^2\ g^{-1}$, 212 $cm^3\ g^{-1}$ and 648 $m^2\ g^{-1}$, and 171 $cm^3\ g^{-1}$ and 511 $m^2\ g^{-1}$, respectively (Fig. 2a). A similar decreasing trend was observed for the pore volume, which measured 0.62 $cm^3\ g^{-1}$, 0.52 $cm^3\ g^{-1}$, 0.32 $cm^3\ g^{-1}$, and 0.26 $cm^3\ g^{-1}$, respectively. Further analysis of pore sizes revealed that **ZSA-1** and **ZSA-3** exhibited two distinct pore diameters, 5.5 Å/8.9 Å and 5.2 Å/8.2 Å, respectively, corresponding to the entrance and interior of the **gis** cage (Fig. S14 and S15). This observation aligns with the methylation-induced modulation along the z direction. Due to the significant steric hindrance imposed by 1,2-DACH in the $x + y$ direction regulation, the pore sizes of **ZSA-12** and **ZSA-13** exhibited considerable contraction. **ZSA-12** displayed two closely spaced pore sizes of 3.9 Å and 4.9 Å, whereas **ZSA-13**, benefiting from ambidextrous fine-tuning along both the $x + y$ and z directions, exhibited a single micropore size of 3.7 Å (Fig. S16 and S17).

The successful modulation of the pore environment in the ZSA platform encourages further investigation into their potential applications in biogas upgrading. Single-component adsorption isotherms of CO_2 and CH_4 were measured for the four ZSAs at 273 K and 298 K. For CO_2, the adsorption capacities of **ZSA-1**, **ZSA-3**, **ZSA-12**, and **ZSA-13** at 273 K and 298 K were 79.1/51.9 $cm^3\ g^{-1}$, 80.4/58.6 $cm^3\ g^{-1}$, 46.1/29.6 $cm^3\ g^{-1}$, and 48.4/38.1 $cm^3\ g^{-1}$, respectively, all demonstrating relatively high CO_2 adsorption (Fig. S18a). Notably, modulation along the $x + y$ direction resulted in **ZSA-13** exhibiting a higher CO_2 adsorption capacity than **ZSA-12** (Fig. 2b). For CH_4, the adsorption capacities of **ZSA-1**, **ZSA-3**, **ZSA-12**, and **ZSA-13** at 273 K and 298 K were 12.2/7.1 $cm^3\ g^{-1}$, 17.1/9.7 $cm^3\ g^{-1}$, 12.1/8.0 $cm^3\ g^{-1}$, and 10.4/5.6 $cm^3\ g^{-1}$, respectively (Fig. S18b). The CH_4 adsorption capacity of **ZSA-13** showed a decreasing trend compared to that of **ZSA-12** due to pore size contraction. Combined with the observed increase in CO_2 adsorption, this suggests that the ambidextrous fine-tuning strategy successfully balances the adsorption capacities of both gases (Fig. 2b).

To further evaluate the interactions between ZSAs and CO_2/CH_4, the adsorption isotherm data were used to derive the isosteric heat of adsorption (Q_{st}). At near-zero loading, all ZSAs exhibited a significantly higher Q_{st} for CO_2 than for CH_4, indicating a stronger affinity for CO_2 (Fig. S19). Further calculations of ΔQ_{st} (the difference in Q_{st} between CO_2 and CH_4) revealed the following trend: **ZSA-13** (24.2 kJ mol^{-1}) > **ZSA-12** (22.2 kJ mol^{-1}) > **ZSA-3** (20.4 kJ mol^{-1}) > **ZSA-1** (20.0 kJ mol^{-1}).

To further evaluate the impact of fine-tuning pore size on CO_2/CH_4 separation, the ideal adsorbed solution theory (IAST) was employed to predict the selectivity of ZSAs for CO_2/CH_4 gas mixtures (compositions of 0.5/0.5 and 0.05/0.95) at 298 K based on experimental isotherms. The dual-site Langmuir–Freundlich equation effectively modeled the data, demonstrating an excellent fit with the isotherms at 298 K ($R^2 > 0.999$) (Fig. S20). The results showed that **ZSA-13** exhibited the highest IAST selectivity, with values of 94.8 (0.5/0.5) and 43.8 (0.05/0.95), surpassing all previously reported HOFs, making it a strong candidate for biogas upgrading (Fig. 2c, d and Table S2). For **ZSA-12**, the IAST selectivity values were 61.2 (0.5/0.5) and 88.9 (0.05/0.95), indicating excellent separation performance under low partial pressure conditions. This is primarily attributed to its strong CO_2 adsorption capacity at low pressure. The IAST selectivity values for **ZSA-1** and **ZSA-3** were 24.5 (0.5/0.5)/33.2 (0.05/0.95) and 27.0 (0.5/0.5)/26.2 (0.05/0.95), respectively, also demonstrating excellent separation performance.

To verify the actual separation performance of **ZSA-12** and **ZSA-13** for biogas produced from different substrate compositions, dynamic breakthrough experiments were conducted. When biogas is derived from carbohydrate fermentation, its CH_4 content is approximately 50–55%. Therefore, dynamic breakthrough experiments were performed under 50/50 conditions at different flow rates. As shown in Fig. 3a, breakthrough experiments with **ZSA-12** were conducted at flow rates of 3 mL min^{-1}, 5 mL min^{-1}, and 7 mL min^{-1}, yielding retention times of 15.7 min g^{-1}, 8.3 min g^{-1}, and 6.7 min g^{-1}, respectively, all demonstrating **ZSA-12**'s high separation efficiency. In contrast, **ZSA-13** exhibited longer retention times at various flow rates, with t values of 22.4 min g^{-1}, 13.1 min g^{-1}, and 9.4 min g^{-1}, showing varying degrees of improvement compared to **ZSA-12** (Fig. 3d). Notably, at a flow rate of 5 mL min^{-1}, the separation efficiency improved by approximately 58%. Furthermore, as shown in Fig. 3b and e, dynamic breakthrough experiments were conducted at a 10/90 ratio, which more closely represents biogas production from lipid-based substrates. **ZSA-12** and **ZSA-13** exhibited retention times of 55.6 min g^{-1} and 63.6 min g^{-1}, further demonstrating their excellent CO_2/CH_4 separation

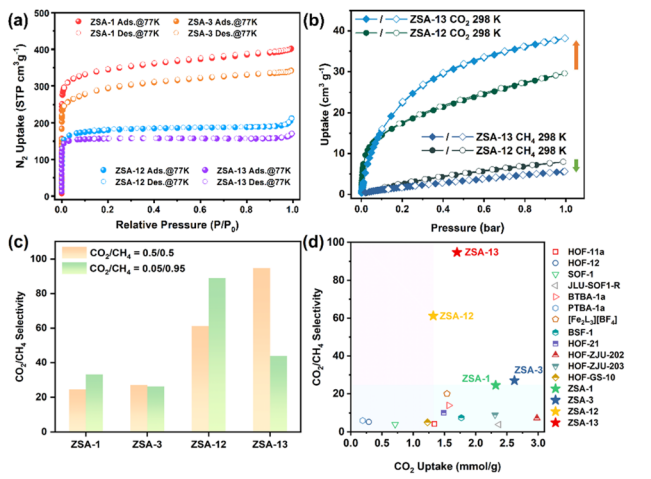

Fig. 2 (a) 77 K N_2 adsorption isotherms of **ZSA-1**, **ZSA-3**, **ZSA-12** and **ZSA-13**; (b) comparison of CO_2 and CH_4 adsorption isotherms of **ZSA-12** and **ZSA-13** at 298 K; (c) IAST selectivity (CO_2/CH_4, 0.5/0.5 and 0.05/0.95) of **ZSA-1**, **ZSA-3**, **ZSA-12** and **ZSA-13** at 298 K and 1 bar; (d) comparison of CO_2/CH_4 (0.5/0.5) selectivity and the CO_2/CH_4 uptake ratio among representative HOFs at 298 K and 1 bar.

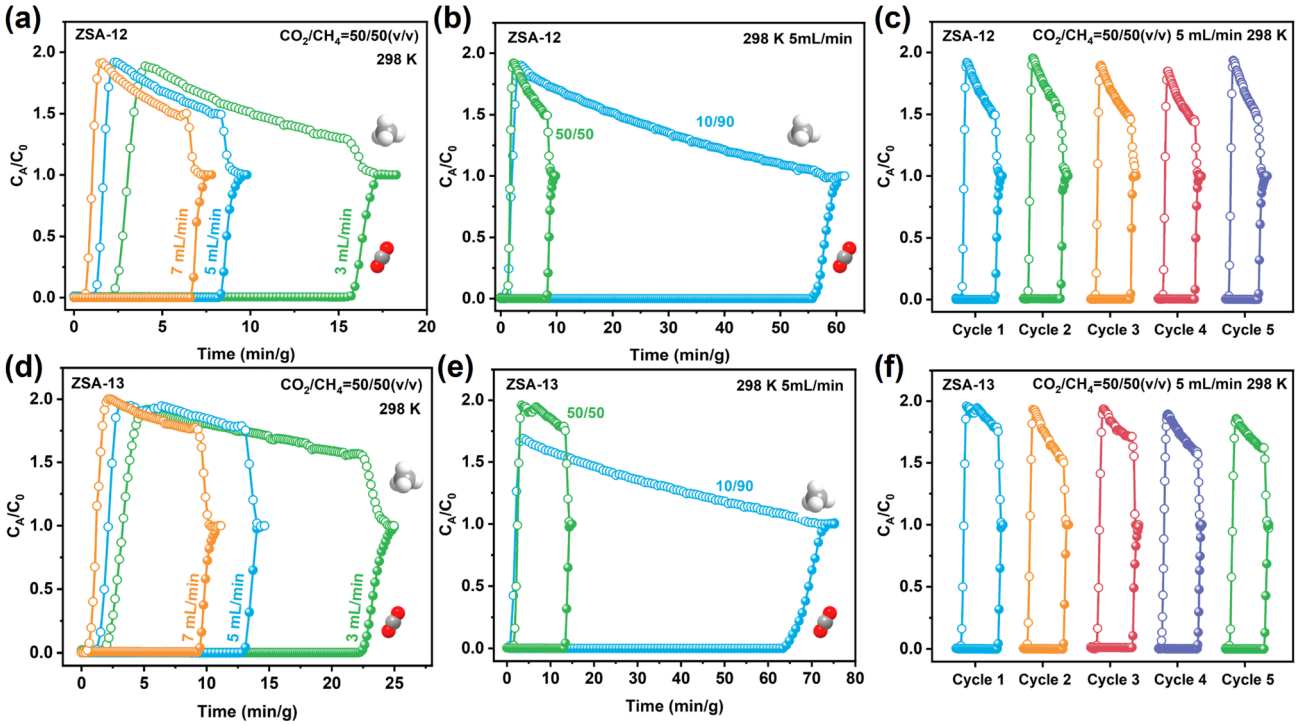

Fig. 3 Experimental breakthrough curves of CO_2/CH_4 with flow rates of 3, 5, and 7 mL min^{-1} (50/50, v/v, 298 K) with (a) **ZSA-12**; (d) **ZSA-13**; experimental breakthrough curves of CO_2/CH_4 with molar ratios of 50/50 and 10/90 with (b) **ZSA-12**; (e) **ZSA-13**; cyclic breakthrough experiments with (c) **ZSA-12**; (f) **ZSA-13**.

capabilities. After five cycles, **ZSA-12** and **ZSA-13** maintained stable separation performance without degradation (Fig. 3c and d). Therefore, **ZSA-12** and **ZSA-13** are promising candidates for CO_2/CH_4 mixture separation.

Simulations and calculations

First-principles based calculations with empirical correction for dispersive interactions were performed to investigate the mechanisms that differentiate CO_2/CH_4 adsorption in **ZSA-1**, **ZSA-3**, **ZSA-12** and **ZSA-13** (Fig. 4 and 5).[44–46] The calculated nearest distance between 2 Co ions is 5.95, 6.03, 5.84 and 6.03 Å for **ZSA-1**, **ZSA-3**, **ZSA-12** and **ZSA-13**, respectively, and is in reasonable agreement with the experimental values of 5.86, 5.94, 5.78 and 5.93 Å, respectively, considering that the average unit cell size of these HOFs are ~20 Å. The reasonable agreement between experimental findings and calculated results suggests that the theoretical approach used is adequate to reproduce the local chemistry within ZSAs of interest.

In the most plausible adsorption structures, CO_2 stays at the opening of the rectangular structure built by 4 Co cations, 4 dicarboxylate ligands and 4 diamine ligands (Fig. 4) and the corresponding E_{ads} is 0.34, 0.38, 0.42 and 0.44 eV, respectively. Upon adsorption, the O–C–O angle within CO_2 is distorted from 180° when freestanding to ~176° after adsorption. CO_2 is stabilized and activated by the C=O moieties within dicarboxylate ligands and the adjacent H of $-CH_3$ moieties. Specifically, in **ZSA-1** and **ZSA-12**, CO_2 is stabilized by the C=O moieties of the same dicarboxylate ligand and the calculated nearest (CO_2)C–O(C=O ligand) distances are 2.98 and 2.82 Å, respectively, in accordance with the change in E_{ads}. In **ZSA-3** and **ZSA-13**, there is a $-CH_3$ on the imidazole moiety of the dicarboxylate ligand which is in reasonable distance from the C=O moieties in the HOFs. In the plausible CO_2 adsorption structure, the minimum (CH_3)H–O(CO_2) distances are 2.57 and 2.59 Å, respectively, and the minimum (CO_2)C–O(C=O ligand) distances are 2.69 and 2.90 Å, in **ZSA-3** and **ZSA-13**, respectively. The increase in CO_2 E_{ads} with respect to **ZSA-1** and **ZSA-12** within **ZSA-3** and **ZSA-13** can thus be attributed to the positive contribution of $-CH_3$ to CO_2 adsorption. The isosurface plots of charge density difference upon CO_2 adsorption also suggest the dispersive nature of CO_2 adsorption with cooperative interactions with both negatively and positively charged centres of adjacent ligands that was previously proposed to account for enhanced CO_2 adsorption in microporous amorphous carbon.[47]

CH_4 staying at the opening of the rectangular structures built up by 4 Co cations, 4 dicarboxylate ligands and 4 diamine ligands was also found to be the most plausible (Fig. 5). The calculated CH_4 E_{ads} is 0.21, 0.23, 0.24 and 0.25 eV for **ZSA-1**, **ZSA-3**, **ZSA-12** and **ZSA-13**, respectively. In these structures, CH_4 uses its 2H to interact mainly with the 4 C=O of 2 dicarboxylate ligands on the opposite edges of the rectangular structure. The average H(CH_4)–O(dicarboxylate ligand) distances are 2.75, 2.71, 2.55 and 2.73 Å, for **ZSA-1**, **ZSA-3**, **ZSA-12** and **ZSA-13**, respectively. The calculated average H(CH_4)–O(dicarboxylate ligand) distances are consistent with the minimum Co–Co distances in these ZSAs. However, the trend is different from

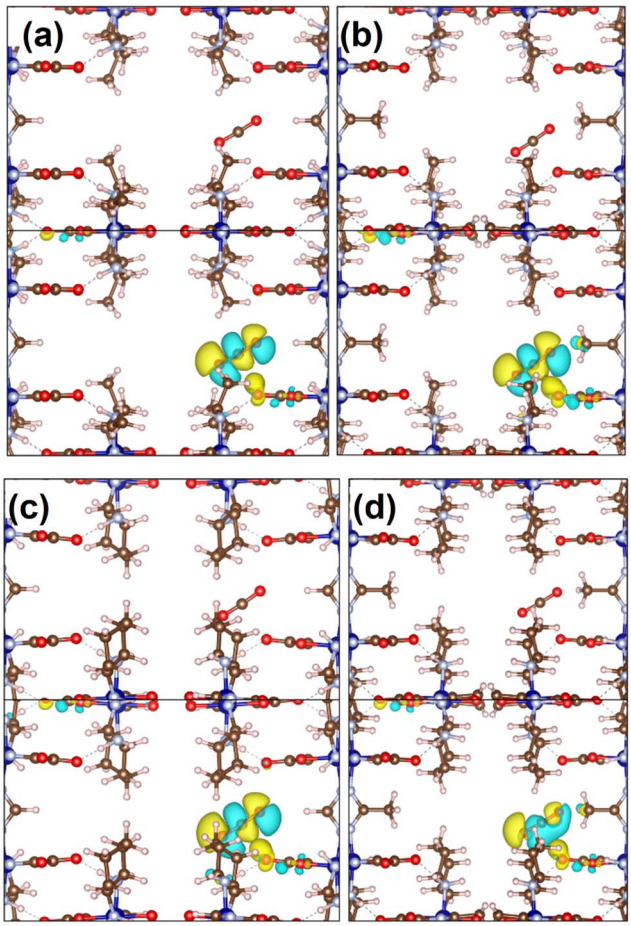

Fig. 4 The most plausible adsorption structures (upper panel) and corresponding isosurface plots of charge density difference (lower panel) of CO_2 in (a) **ZSA-1**, (b) **ZSA-3**, (c) **ZSA-12** and (d) **ZSA-13** viewed along the *b*-axis; in (a–d), C, N, Co, H and O atoms are in brown, light blue, dark blue, light pink and red, respectively, the charge accumulation and charge depletion regions are in yellow and blue, respectively, and the isovalues are ±0.0005 a.u.

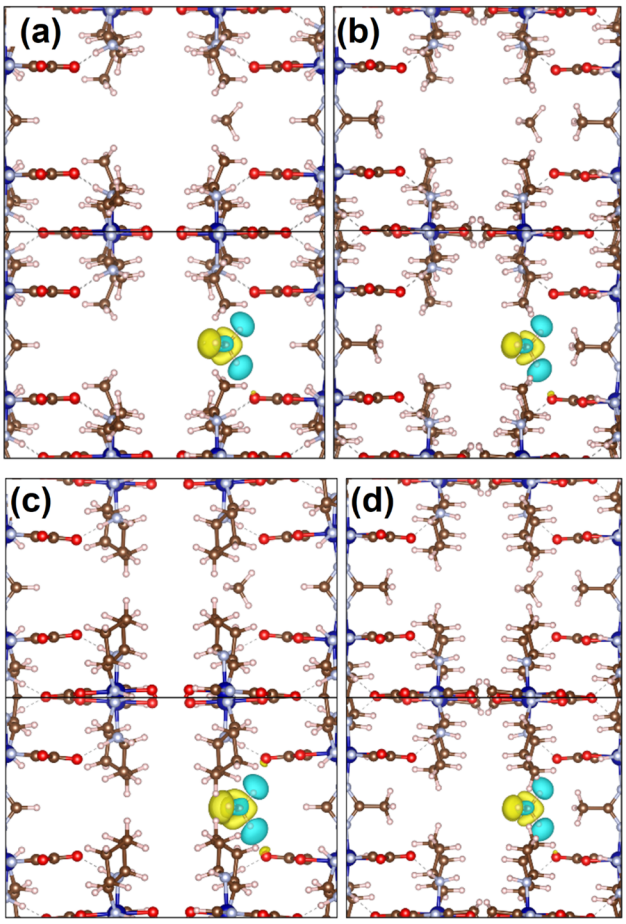

Fig. 5 The most plausible adsorption structures (upper panel) and corresponding isosurface plots of charge density difference (lower panel) of CH_4 in (a) **ZSA-1**, (b) **ZSA-3**, (c) **ZSA-12** and (d) **ZSA-13** viewed along the *b*-axis. In (a–d), C, N, Co, H and O atoms are in brown, light blue, dark blue, light pink and red, respectively, the charge accumulation and charge depletion regions are in yellow and blue, respectively, and the isovalues are ±0.0005 a.u.

that of CH_4 E_{ads}, showing the complex nature of the adsorption. The calculated isosurface plots of charge density difference upon adsorption show that the degree of charge transfer is mainly within CH_4 and the charge transfer is more severe for **ZSA-13** with a superior E_{ads}. This also indicates that the adsorption of CH_4 is mainly dispersive. With the calculated E_{ads} of both CO_2 and CH_4, we moved on to evaluate the difference between CO_2 and CH_4 E_{ads} (ΔE_{ads}) as the driving force for CO_2/CH_4 mixture separation with the ZSAs. The larger the ΔE_{ads}, the better the separation performance of HOF materials. The calculated ΔE_{ads} of **ZSA-1**, **ZSA-3**, **ZSA-12** and **ZSA-13** is 0.13, 0.16, 0.18 and 0.19 eV, respectively. In this sense, **ZSA-13** would demonstrate a much better CO_2/CH_4 separation performance, and this is in excellent agreement with the aforementioned experimental analysis.

Stability and scalability

In addition to separation performance, thermal and chemical stability are crucial for practical applications. The synthesized **ZSA-12** and **ZSA-13** were immersed in solutions of varying pH for 24 hours, followed by filtration and subsequent PXRD and gas adsorption measurements. The diffraction patterns (Fig. 6a and b) and N_2 isotherms (Fig. 6c and d) remained virtually unchanged, indicating that **ZSA-12** and **ZSA-13** exhibit exceptional chemical stability even in solutions with pH = 2 and pH = 12, which surpasses that of most HOFs. Notably, even after long-term exposure to air for 3 months followed by treatment in aqueous solution at pH = 1 for 12 hours, no significant changes were observed in PXRD patterns, further demonstrating their outstanding structural robustness (Fig. S22). This robust chemical stability is likely attributed to the presence of saturated coordination bonds, multiple hydrogen bonding interactions, and its ultramicroporous structure. Furthermore, variable-temperature PXRD analysis confirms that **ZSA-12** and **ZSA-13** remain stable at temperatures up to 300 °C (Fig. S23 and S24).

The commercialization prospects of HOFs have garnered increasing attention with their rapid development. For

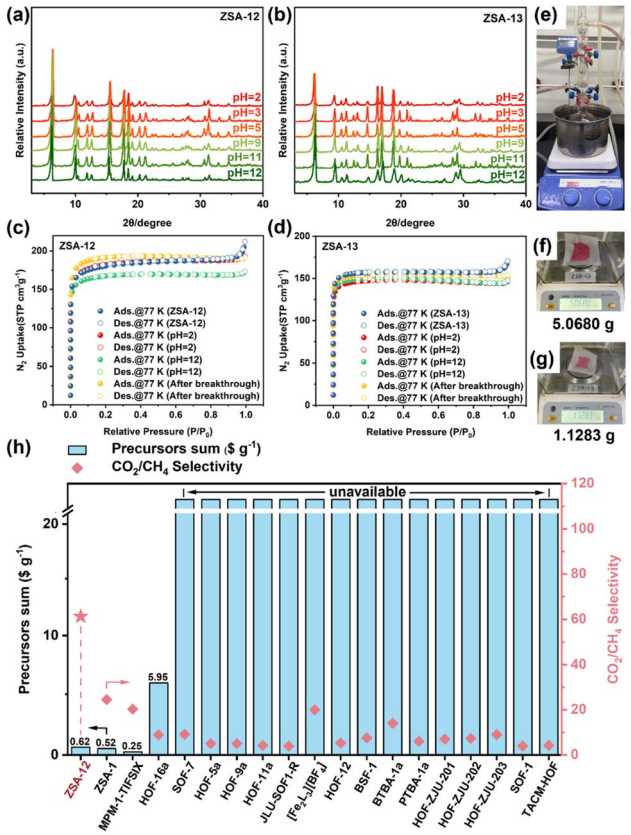

Fig. 6 Evaluation of chemical stability of **ZSA-12** and **ZSA-13** *via* (a and b) PXRD and (c and d) 77 K N_2 adsorption measurements; (e) diagram of the gram-scale synthesis setup in water; samples obtained through synthesis: (f) **ZSA-12**, and (g) **ZSA-13**; (h) comparison of **ZSA-12** with other HOFs in terms of separation performance and synthesis cost.

commercialization, their production cost must be acceptable, and synthesis optimization must be scaled from laboratory to industrial levels, ideally under environmentally friendly conditions. IAST calculations and breakthrough experiments have confirmed that **ZSA-12** and **ZSA-13** exhibit excellent CO_2/CH_4 separation capabilities. Moreover, the low-cost ligands and mild synthetic conditions required for the synthesis of **ZSA-12** and **ZSA-13** enable us to explore their scale-up synthesis. **ZSA-12** and **ZSA-13** can be synthesized on a gram scale simply by stirring under hydrothermal conditions. For **ZSA-12**, which has more readily accessible ligands, synthesis at the 5 g scale was achieved, and the resulting PXRD pattern matches well with the simulated PXRD (Fig. 6e–g, S25 and 26). The precursors for **ZSA-12** are readily available at low cost in the market, with a synthesis cost as low as \$0.62 per gram. Compared to other HOFs used for similar separation tasks, it is a rare and cost-effective HOF with commendable separation performance (Fig. 6h).

Conclusions

In summary, by constructing the ZSA platform and the ambidextrous fine-tuning strategy, we successfully synthesized two isoreticular HOFs, **ZSA-12** and **ZSA-13**. Both compounds exhibit permanent porosity and distinct pore sizes, which are determined by the dimensions of the functionalized ligand and diamine linker. **ZSA-12** and **ZSA-13** demonstrated outstanding CO_2/CH_4 separation selectivity, surpassing all previously reported HOFs. Moreover, both compounds exhibited exceptional thermal and chemical stability, maintaining excellent separation performance in cyclic breakthrough experiments. This series of ZSAs provides a novel strategy for constructing isoreticular HOFs, and their simple and cost-effective scalable synthesis highlights their potential for practical biogas upgrading applications in the future.

Experimental

Synthesis of ZSA-1

ZSA-1 was synthesized following the reported method.[41] A mixture of 4,5-imidazoledicarboxylic acid (H_3ImDC, 0.040 g, 0.25 mmol), $Co(CH_3COO)_2\cdot 4H_2O$ (0.060 g, 0.25 mmol), H_2O (3 mL), and 1,2-propanediamine (1,2-PDA, 0.060 mL) was sealed in a Teflon-lined stainless steel autoclave, heated at 120 °C for 24 h, and then cooled to room temperature. The red polyhedral crystals were isolated, washed with distilled water, and dried in air (63% yield based on $Co(CH_3COO)_2\cdot 4H_2O$).

Synthesis of ZSA-3

ZSA-3 was synthesized following the reported method.[48] A mixture of 2-methyl-1*H*-imidazole-4,5-dicarboxylic acid (H_3-MeImDC, 0.040 g, 0.25 mmol), $Co(CH_3COO)_2\cdot 4H_2O$ (0.060 g, 0.25 mmol), H_2O (3 mL), and 1,2-propanediamine (1,2-PDA, 0.060 mL) was sealed in a Teflon-lined stainless steel autoclave, heated at 120 °C for 24 h, and then cooled to room temperature. The red polyhedral crystals were isolated, washed with distilled water, and dried in air (68% yield based on $Co(CH_3COO)_2\cdot 4H_2O$).

Synthesis of ZSA-12

A mixture of 4,5-imidazoledicarboxylic acid (H_3ImDC, 0.020 g, 0.125 mmol), $Co(CH_3COO)_2\cdot 4H_2O$ (0.030 g, 0.125 mmol), H_2O (5 mL), and 1,2-diaminocyclohexane (1,2-DACH, 0.060 mL) was sealed in a Teflon-lined stainless steel autoclave, heated at 120 °C for 24 hours, and then cooled to room temperature. The red polyhedral crystals were isolated and purified through washing with distilled water, followed by drying in air (70% yield based on $Co(CH_3COO)_2\cdot 4H_2O$).

Synthesis of ZSA-13

A mixture of 2-methyl-1*H*-imidazole-4,5-dicarboxylic acid (H_3-MeImDC, 0.020 g, 0.125 mmol), $Co(CH_3COO)_2\cdot 4H_2O$ (0.030 g, 0.125 mmol), H_2O (5 mL), and 1,2-diaminocyclohexane (1,2-DACH, 0.060 mL) was sealed in a Teflon-lined stainless steel autoclave, heated at 120 °C for 24 h, and then cooled to room temperature. The red polyhedral crystals were isolated, washed with distilled water, and dried in air (62% yield based on $Co(CH_3COO)_2\cdot 4H_2O$).

Scale-up process of ZSA-12

A mixture of 4,5-imidazoledicarboxylic acid (H_3ImDC, 3 g, 18.75 mmol), $Co(CH_3COO)_2 \cdot 4H_2O$ (4.5 g, 18.75 mmol), H_2O (300 mL), and 1,2-diaminocyclohexane (1,2-DACH, 9 mL) was packed into a 500 mL reagent bottle, and heated at 120 °C for 72 hours. The red power crystals were isolated and purified through washing with distilled water and ethanol, followed by drying in air (68% yield based on $Co(CH_3COO)_2 \cdot 4H_2O$).

Scale-up process of ZSA-13

A mixture of 2-methyl-1*H*-imidazole-4,5-dicarboxylic acid (H_3-MeImDC, 1 g, 6.25 mmol), $Co(CH_3COO)_2 \cdot 4H_2O$ (1.5 g, 6.25 mmol), H_2O (100 mL), and 1,2-diaminocyclohexane (1,2-DACH, 3 mL) was packed into a 250 mL reagent bottle, and heated at 120 °C for 72 hours. The red power crystals were isolated and purified through washing with distilled water and ethanol, followed by drying in air (45% yield based on $Co(CH_3COO)_2 \cdot 4H_2O$).

Author contributions

Baobing Tang: preparation and synthesis of materials, experimental data analysis, writing – original draft; Xueyue Yu: experimental data analysis, writing – original draft; Guanghua Li: experimental data analysis; Xin Liu: experimental data analysis, resources, software; Jiantang Li: writing – review & editing, supervision, data curation; Yunling Liu: writing – review & editing, supervision.

Conflicts of interest

There are no conflicts to declare.

Data availability

The authors confirm that the data supporting the findings of this study are available within the article and/or its SI.

Supplementary information available: structural information, PXRD and TGA analysis characterizations, and gas adsorption and separation. See DOI: **https://doi.org/10.1039/d5sc02892b**.

Crystallographic data for ZSA-12, **ZSA-13** haves been deposited at the CCDC under 2436269 and, 2436268.[49,50]

Acknowledgements

This work was supported by the National Natural Science Foundation of China (No. 22171100, 21771029, 22301154, 11811530631, 21573034 and U23A20360), the Jinhua City Project (2024-4-018), the Zhejiang Provincial Natural Science Foundation of China (LMS25B010002) and the '111 Center' (B17020). The supercomputer time was provided by the High Performance Computing Center at Dalian University of Technology.

Notes and references

1 A. Roozitalab, F. Hamidavi and A. Kargari, A review of membrane material for biogas and natural gas upgrading, *Gas Sci. Eng.*, 2023, **114**, 204969.
2 J. B. Holm-Nielsen, T. Al Seadi and P. Oleskowicz-Popiel, The future of anaerobic digestion and biogas utilization, *Bioresour. Technol.*, 2009, **100**, 5478–5484.
3 M. Yusuf, R. Kumar, M. Ali Khan, M. J. Ahmed, M. Otero, S. Muthu Prabhu, M. Son, J.-H. Hwang, W. Hyoung Lee and B.-H. Jeon, Metal-organic framework-based composites for biogas and natural gas uptake: An overview of adsorption and storage mechanisms of gaseous fuels, *Chem. Eng. J.*, 2023, **478**, 147302.
4 C. E. Wylock and W. M. Budzianowski, Performance evaluation of biogas upgrading by pressurized water scrubbing via modelling and simulation, *Chem. Eng. Sci.*, 2017, **170**, 639–652.
5 X.-W. Yan, F. Bigdeli, M. Abbasi-Azad, S.-J. Wang and A. Morsali, Selective separation of CO_2/CH_4 gases by metal-organic framework-based composites, *Coord. Chem. Rev.*, 2024, **520**, 216126.
6 R. Wei, T. Alshahrani, B. Chen, A. B. Ibragimov, H. Xu and J. Gao, Advances in porous materials for efficient separation and purification of flue gas, *Sep. Purif. Technol.*, 2025, **352**, 128238.
7 J. Li, Z. Song, X. Zhou, X. Wang, M. Feng, D. Wang and B. Chen, Reticular chemistry guided function customization: a case study of constructing low-polarity channels for efficient C_3H_6/C_2H_4 separation, *Chem. Sci.*, 2025, **16**, 7411–7417.
8 C. Jiang, J. X. Wang, D. Liu, E. Wu, X. W. Gu, X. Zhang, B. Li, B. Chen and G. Qian, Supramolecular Entanglement in a Hydrogen-Bonded Organic Framework Enables Flexible-Robust Porosity for Highly Efficient Purification of Natural Gas, *Angew. Chem., Int. Ed.*, 2024, **63**, e202404734.
9 Y. Chen, X. Chen, L. Li, X. Chen, J. Xia and L. Zhang, A triply linked propellane-nanoring hybrid serving as a good host, *Chem. Sci.*, 2025, **16**, 6822–6827.
10 J. Zhang, H. Zheng, F. Chen, Z. Wang, H. Li, F. Sun, D. Zhao, V. Valtchev, S. Qiu and Q. Fang, High-Connectivity 3D Covalent Organic Frameworks with pdp Net for Efficient C_2H_2/CO_2 Separation, *Angew. Chem., Int. Ed.*, 2025, e202500161, DOI: **10.1002/anie.202500161**.
11 S. Y. Li, Y. Y. Xue, J. W. Wang, H. P. Li, J. Lei, H. J. Lv, X. Bu, P. Zhang, Y. Wang, W. Y. Yuan and Q. G. Zhai, Metal-organic frameworks with two different-sized aromatic ring-confined nanotraps for benchmark natural gas upgrade, *Chem. Sci.*, 2024, **15**, 17547–17555.
12 S. Lin, Y. Liang, P. Ke, L. Wang, D. Chen, L. Zhang and Y. He, Efficient Methane Purification Using a Robust and Recoverable Hydrogen-Bonded Organic Framework, *Angew. Chem., Int. Ed.*, 2025, **64**, e202500970.
13 J. X. Wang, J. Pei, X. W. Gu, Y. X. Lin, B. Li and G. Qian, Efficient CO_2/CO separation in a stable microporous

hydrogen-bonded organic framework, *Chem. Commun.*, 2021, **57**, 10051–10054.
14 R. B. Lin, Y. He, P. Li, H. Wang, W. Zhou and B. Chen, Multifunctional porous hydrogen-bonded organic framework materials, *Chem. Soc. Rev.*, 2019, **48**, 1362–1389.
15 J. Li and B. Chen, Flexible hydrogen-bonded organic frameworks (HOFs): opportunities and challenges, *Chem. Sci.*, 2024, **15**, 9874–9892.
16 Y. Wang, J. Yao, S. Wu, C. Zhi, L. Yin, Z. Song, J. Wang, L. Ling, Y. Ma, D. Zhang, J. Li, L. Li and B. Chen, Encapsulation of metal nanoclusters into hydrogen-bonded organic frameworks for double-response-reverse ammonia fluorescence sensing, *Chem*, 2025, 102457.
17 Y. Li, H. Chen, J. Huang, H. Zhang, S. Lin, Z. M. Ye, S. Xiang, B. Chen and Z. Zhang, Self-Healing B ← N-Based Hydrogen-Bonded Organic Framework for Exclusive Recognition and Separation of Toluene from Methyl-Cyclohexane, *J. Am. Chem. Soc.*, 2024, **146**, 19425–19433.
18 X. Song, Y. Wang, C. Wang, X. Gao, Y. Zhou, B. Chen and P. Li, Self-Healing Hydrogen-Bonded Organic Frameworks for Low-Concentration Ammonia Capture, *J. Am. Chem. Soc.*, 2024, **146**, 627–634.
19 H. Zhao, B. Fan, S. Hu, X. Liu, B. Tang and P. Xue, Guest-triggered gate-opening of flexible hydrogen-bonded framework for separation of styrene and ethylbenzene, *Chin. Chem. Lett.*, 2025, 111005.
20 L. Li, X. Zhang, X. Lian, L. Zhang, Z. Zhang, X. Liu, T. He, B. Li, B. Chen and X. H. Bu, Flue gas desulfurization and SO_2 recovery within a flexible hydrogen-bonded organic framework, *Nat. Chem.*, 2025, **17**, 727–733.
21 L. He, Y. Li, L. Li, Z. Wang, Y. Chen, F. Yuan, G. Lan, C. Chen, S. Xiang, B. Chen and Z. Zhang, A Microporous Hydrogen-Bonded Organic Framework with Open Pyrene Sites Isolated by Hydrogen-Bonded Helical Chains for Efficient Separation of Xenon and Krypton, *Angew. Chem., Int. Ed.*, 2025, **64**, e202418917.
22 Y. Yang, L. Li, R. B. Lin, Y. Ye, Z. Yao, L. Yang, F. Xiang, S. Chen, Z. Zhang, S. Xiang and B. Chen, Ethylene/ethane separation in a stable hydrogen-bonded organic framework through a gating mechanism, *Nat. Chem.*, 2021, **13**, 933–939.
23 Y. Chen, Y. Yang, Y. Wang, Q. Xiong, J. Yang, S. Xiang, L. Li, J. Li, Z. Zhang and B. Chen, Ultramicroporous Hydrogen-Bonded Organic Framework Material with a Thermoregulatory Gating Effect for Record Propylene Separation, *J. Am. Chem. Soc.*, 2022, **144**, 17033–17040.
24 W. Wang, Y. Shi, W. Chai, K. W. K. Tang, I. Pyatnitskiy, Y. Xie, X. Liu, W. He, J. Jeong, J. C. Hsieh, A. R. Lozano, B. Artman, X. Shi, N. Hoefer, B. Shrestha, N. B. Stern, W. Zhou, D. W. McComb, T. Porter, G. Henkelman, B. Chen and H. Wang, H-bonded organic frameworks as ultrasound-programmable delivery platform, *Nature*, 2025, **638**, 401–410.
25 D. Yu, H. Zhang, X. Du, J. Ren and X. Qu, Hydrogen-Bonded Organic Framework-Based NIR-II Activated Hydrogen Production for Treatment of Alzheimer's Disease Model Mice, *Small*, 2025, **21**, e2410063.
26 Y. Pan, F. Zeng, X. Luan, G. He, S. Qin, Q. Lu, B. He, X. Han and Y. Song, Polyamine-Depleting Hydrogen-Bond Organic Frameworks Unleash Dendritic Cell and T Cell Vigor for Targeted CRISPR/Cas-Assisted Cancer Immunotherapy, *Adv. Mater.*, 2025, **37**, e2411886.
27 L. Gu, H. Wu, X. Li, J. Xu, M. Wang, C. Li, L. Yao, Y. Diao, Y. Li, F. Chen, F. Shen, H. Xiang, Y. Chen and T. Yang, Hydrogen-Bonded Organic Framework Nanoscintillators for X-Ray-Induced Photodynamic Therapy in Hepatocellular Carcinoma, *Adv. Mater.*, 2025, **37**, e2417001.
28 C. Ma, L. Qin, T. Zhou and J. Zhang, Customized structures of hydrogen-bonded organic frameworks towards photocatalysis, *Energy Environ. Sci.*, 2024, **17**, 8992–9026.
29 L. Wang, J. Deng, S. Bai, Y. Wu and W. Zhu, Enhanced Photocatalytic Degradation Performance by Micropore-Confined Charge Transfer in Hydrogen-Bonded Organic Framework-Like Cocrystals, *Small*, 2024, **20**, e2406352.
30 M. Zhou, D. Ding, Y. Shi, K. Wang, Q. Wang, X. Chen, H.-M. Shen, T.-S. Zhang, Y.-F. Yang, J. Xia, H. Li and Y. She, Hydrogen-Bonded organic framework Containing stacked Cu^{2+} for photocatalytic reduction of CO_2 to C_2H_4, *Chem. Eng. J.*, 2025, **503**, 158501.
31 A. Chauhan, R. Kumar, P. Raizada, S. Thakur, V.-H. Nguyen, A. Singh, Q. Van Le, P. Singh and A. Sudhaik, Novel hydrogen-bonded organic framework (HOF) for highly efficient photocatalysis: From structural designs to multifunctional applications, *Coord. Chem. Rev.*, 2025, **535**, 216634.
32 L. Chen, B. Zhang, L. Chen, H. Liu, Y. Hu and S. Qiao, Hydrogen-bonded organic frameworks: design, applications, and prospects, *Mater. Adv.*, 2022, **3**, 3680–3708.
33 H. Wang, B. Li, H. Wu, T. L. Hu, Z. Yao, W. Zhou, S. Xiang and B. Chen, A Flexible Microporous Hydrogen-Bonded Organic Framework for Gas Sorption and Separation, *J. Am. Chem. Soc.*, 2015, **137**, 9963–9970.
34 Z. J. Lin, J. Y. Qin, X. P. Zhan, K. Wu, G. J. Cao and B. Chen, Robust Mesoporous Functional Hydrogen-Bonded Organic Framework for Hypochlorite Detection, *ACS Appl. Mater. Interfaces*, 2022, **14**, 21098–21105.
35 Z.-W. Li, Z.-J. Huang, Y.-X. Li, X. Wu, W. Shi, Y.-B. Zhang, X. Ma, G. Ouyang, B.-H. Ye, G.-F. Liu and X.-M. Chen, An Ultrastable, Easily Scalable and Regenerable Macrocycle-Based Hydrogen-Bonded Organic Framework, *CCS Chem.*, 2025, **7**, 293–306.
36 M. Vicent-Morales, M. Esteve-Rochina, J. Calbo, E. Orti, I. J. Vitorica-Yrezabal and G. Minguez Espallargas, Semiconductor Porous Hydrogen-Bonded Organic Frameworks Based on Tetrathiafulvalene Derivatives, *J. Am. Chem. Soc.*, 2022, **144**, 9074–9082.
37 X.-J. Xi, Z. Ji, F. Lang, Z. Di, Y. Li, C. Li, H. Zhang, L. Zeng, J. Pang, M. Wu and X.-H. Bu, Pore engineering in highly stable hydrogen-bonded organic frameworks for efficient CH_4 purification, *Chem. Eng. J.*, 2024, **497**, 154420.
38 A. Karmakar, R. Illathvalappil, B. Anothumakkool, A. Sen, P. Samanta, A. V. Desai, S. Kurungot and S. K. Ghosh, Hydrogen-Bonded Organic Frameworks (HOFs): A New

Class of Porous Crystalline Proton-Conducting Materials, *Angew. Chem., Int. Ed.*, 2016, **55**, 10667–10671.

39 Z. Bao, D. Xie, G. Chang, H. Wu, L. Li, W. Zhou, H. Wang, Z. Zhang, H. Xing, Q. Yang, M. J. Zaworotko, Q. Ren and B. Chen, Fine Tuning and Specific Binding Sites with a Porous Hydrogen-Bonded Metal-Complex Framework for Gas Selective Separations, *J. Am. Chem. Soc.*, 2018, **140**, 4596–4603.

40 J. Lei, W. Yuan, Y.-Y. Xue, L. Li, T. Lan, Y.-F. Li, Z.-L. Zhong and Q.-G. Zhai, Scalable reflux synthesis of a bimicroporous hydrogen-bonded framework with specific molecule recognition ability for one-step ethylene purification, *J. Mater. Chem. A*, 2025, **13**, 7347–7356.

41 S. Wang, T. Zhao, G. Li, L. Wojtas, Q. Huo, M. Eddaoudi and Y. Liu, From metal-organic squares to porous zeolite-like supramolecular assemblies, *J. Am. Chem. Soc.*, 2010, **132**, 18038–18041.

42 X. Chen, R. K. Huang, K. Takahashi, S. I. Noro, T. Nakamura and I. Hisaki, A Proton Conductive Porous Framework of an 18-Crown-6-Ether Derivative Networked by Rigid Hydrogen Bonding Modules, *Angew. Chem., Int. Ed.*, 2022, **61**, e202211686.

43 B. Li, W. Qiu, G. P. A. Yap, Y. L. Dory and J. P. Claverie, Hydrogen-Bonded Organic Frameworks Based on Endless-Stacked Amides for Iodine Capture and Detection, *Adv. Funct. Mater.*, 2023, **34**, 2311964.

44 G. Kresse and J. Furthmuller, Efficient iterative schemes for ab initio total-energy calculations using a plane-wave basis set, *Phys. Rev. B: Condens. Matter Mater. Phys.*, 1996, **54**, 11169–11186.

45 E. R. Johnson and A. D. Becke, A post-Hartree-Fock model of intermolecular interactions: inclusion of higher-order corrections, *J. Chem. Phys.*, 2006, **124**, 174104.

46 S. Grimme, J. Antony, S. Ehrlich and H. Krieg, A consistent and accurate ab initio parametrization of density functional dispersion correction (DFT-D) for the 94 elements H-Pu, *J. Chem. Phys.*, 2010, **132**, 154104.

47 Y. Zhao, X. Liu, K. X. Yao, L. Zhao and Y. Han, Superior Capture of CO_2 Achieved by Introducing Extra-framework Cations into N-doped Microporous Carbon, *Chem. Mater.*, 2012, **24**, 4725–4734.

48 S. Wang, Y. Belmabkhout, A. J. Cairns, G. Li, Q. Huo, Y. Liu and M. Eddaoudi, Tuning Gas Adsorption Properties of Zeolite-like Supramolecular Assemblies with gis Topology via Functionalization of Isoreticular Metal-Organic Squares, *ACS Appl. Mater. Interfaces*, 2017, **9**, 33521–33527.

49 B. Tang, X. Yu, G. Li, X. Liu, J. Li and Y. Liu, 2025, DOI: **10.5517/ccdc.csd.cc2ms49w**.

50 B. Tang, X. Yu, G. Li, X. Liu, J. Li and Y. Liu, 2025, DOI: **10.5517/ccdc.csd.cc2ms4bx**.